# Robust Detection of Retinal Neovascularization in Widefield Optical Coherence Tomography

JINYI HAO, $^1$  JIE WANG, $^1$  KOTARO TSUBOI, $^2$  LIQIN GAO, $^1$  TRISTAN T. HORMEL, $^1$  YUKUN GUO, $^{1,3}$  AN-LUN WU, $^{1,4}$  MIN GAO, $^{1,3}$  CHRISTINA J. FLAXEL, $^1$  STEVEN T. BAILEY, $^1$  THOMAS S. HWANG, $^1$  YALI JIA $^{1,3,*}$ 

<sup>1</sup>Casey Eye Institute, Oregon Health & Science University, Portland, Oregon 97239, USA

Abstract: Retinal neovascularization (RNV) is a vision threatening development in diabetic retinopathy (DR). Vision loss associated with RNV is preventable with timely intervention, making RNV clinical screening and monitoring a priority. Optical coherence tomography (OCT) angiography (OCTA) provides high-resolution imaging and high-sensitivity detection of RNV lesions. With recent commercial devices introducing widefield OCTA imaging to the clinic, the technology stands to improve early detection of RNV pathology. However, to meet clinical requirements these imaging capabilities must be combined with effective RNV detection and quantification, but existing algorithms for OCTA images are optimized for conventional, i.e. narrow, fields of view. Here, we present a novel approach for RNV diagnosis and staging on widefield OCT/OCTA. Unlike conventional methods dependent on multi-layer retinal segmentation, our model reframes RNV identification as a direct binary localization task. Our fully automated approach was trained and validated on 589 widefield scans (17×17mm to 26×21-mm) collected from multiple devices at multiple clinics. Our method achieved a device-dependent area under curve (AUC) ranging from 0.96 to 0.99 for RNV diagnosis, and mean intersection over union (IOU) ranging from 0.76 to 0.88 for segmentation. We also demonstrate our method's ability to monitor lesion growth longitudinally. Our results indicate that deep learning-based analysis for widefield OCTA images could offer a valuable means for improving RNV screening and management.

## 1. Introduction

Diabetic retinopathy (DR) is the leading cause of preventable blindness among the working-age population worldwide [1, 2]. In proliferative diabetic retinopathy (PDR) RNV emerges as a hallmark pathological feature that can lead to severe vision loss due to vitreous hemorrhage or tractional retinal detachment [3]. A key anatomical structure involved in this process is the vitreoretinal interface (VRI), which acts as the boundary between the retina and the vitreous. The penetration of RNV through the VRI marks a critical transition in disease progression, enabling pathological vessels to extend into the vitreous cavity. This disruption significantly increases the risk of vision-threatening complications, underscoring the need for timely clinical intervention to halt progression and preserve vision [4, 5]. But for timely intervention we require highly sensitive screening and monitoring techniques.

Optimal RNV management requires an imaging modality that can effectively visualize even small RNV lesions, which can occur throughout the retina. Widefield optical coherence tomography (OCT) and OCT angiography (OCTA). Standard OCT reveals retinal structural information such as alterations above the VRI that are associated with RNV [6]. OCTA is generated by measuring motion contrast between OCT cross-sections, which highlights retinal

<sup>&</sup>lt;sup>2</sup>Department of Ophthalmology, Aichi Medical University, 1-1, Yazako Karimata, Nagakute, Aichi, 480-1195, Japan

<sup>&</sup>lt;sup>3</sup>Department of Biomedical Engineering, Oregon Health & Science University, Portland, Oregon 97239, USA

<sup>&</sup>lt;sup>4</sup>Department of Ophthalmology, Mackay Memorial Hospital, Hsinchu 300044, Taiwan \*jiaya@ohsu.edu

vasculature [7, 8], and can be acquired simultaneously with OCT. Moreover, widefield OCTA is capable of detecting subclinical RNV, and measurements of RNV lesion complexity and area on OCTA have been shown to correlate with treatment response [9]. Finally, both widefield OCT and OCTA are noninvasive, rapid, and cost-effective, making them well-suited for screening.

In addition to an imaging modality capable to accurately identifying RNV, screening and monitoring also require automated image analysis procedures for diagnosis and monitoring. Deep learning has already facilitated automated detection, segmentation, and quantification of RNV and other vascular abnormalities on OCTA images [10-12]. However, these results were achieved on small fields of view (FOV), a traditional limitation in OCTA imaging that has recently been ameliorated by devices that can obtain much larger FOV images ( $26 \times 21$ -mm for DREAM OCT, for example, compared to earlier devices that typically obtained  $6 \times 6$ -mm FOVs in a single shot at most). RNV detection in widefield OCTA is more challenging. To begin with, retinal anatomy differs from the posterior pole to the periphery, which requires algorithms to be context sensitive. This anatomic variation has several aspects, including thinning of some tissue layers and merging of some plexuses. Of particular importance is the eye's curvature, which introduces axial variation in the scanning region. Furthermore, optical aberrations present in the periphery degrade image quality through blurring (loss of contrast and resolution). These are complications that must be addressed in an effective RNV detection solution for widefield imaging.

In this study, we propose a fully automated deep learning framework that can successfully detect and segment RNV in widefield OCT/OCTA scans. To accommodate the morphological variability of RNV, the entire vitreous is designated as the detection zone, rather than relying on a fixed height slab as in previous methods [13, 14]. The framework adopts a two-stage approach: the first stage performs accurate VRI segmentation in order to identify the vitreous, while the second stage jointly analyzes *en face* OCTA and OCT images to identify and segment RNV lesions. The proposed method is validated on a multi-device OCTA dataset comprising images acquired from two clinics and three imaging systems with varying fields of view, demonstrating its generalizability and robustness for fully automated RNV analysis.

## 2. Methods

#### 2.1 Data set

In this study, OCT/OCTA scans were collected using three commercial imaging platforms at two eye institutes, the Casey Eye Institute, Oregon Health & Science University, (Portland, OR, USA); and the Department of Ophthalmology, Aichi Medical University (Nagakute, Japan). The Solix (Visionix/Optovue Inc., Fremont, CA, USA), is a spectral-domain platform operating at a 120-kHz axial scan rate and centered at an 840-nm wavelength. It acquires four 9 × 9-mm OCT/OCTA volumes at different retinal locations, collectively covering approximately a 17 × 17-mm region that includes the superotemporal (ST), superonasal (SN), inferotemporal (IT), and inferonasal (IN) regions. Each set acquired within approximately 5 minutes. Each volume scan consists of 600 B-scans, with each B-scan comprising 600 A-scans, resulting in a transverse sampling density of 600 × 600-pixels per volume [15]. The DREAM OCT (Intalight Inc., San Jose, CA, USA) is a swept-source widefield OCTA platform designed for efficient single-shot acquisition. It captures 26 × 21-mm OCTA scans in a single acquisition session lasting around two minutes, including both acquisition and processing time. This approach simplifies imaging for patients with poor fixation and is well suited for clinical workflows, though it involves some degree of down sampling [16]. The S1-OCTA (Canon Inc., Tokyo, Japan) is a 100-kHz swept-source OCTA device operating over a wavelength range of 1010-1160 nm. For each participant, a 23 × 20-mm widefield OCTA image was acquired, centered on the fovea, to capture a large retinal area with deep tissue penetration [17].

The dataset comprised both RNV-positive and non-RNV control cases. All RNV cases were clinically confirmed by retinal specialists based on multimodal imaging and clinical diagnosis. The non-RNV control group consisted of both healthy eyes and eyes diagnosed with other retinal conditions, including age-related macular degeneration (AMD), non-neovascular diabetic retinopathy, and branch retinal vein or artery occlusion (BRVO/BRAO), each confirmed by clinical examination. For non-RNV controls only one eye was imaged per volunteer. For RNV cases, both eyes were included if both presented with RNV, otherwise only the eye with RNV was used in the dataset. Furthermore, for patients with longitudinal imaging records, each follow-up scan was treated as an independent case due to morphological changes between visits. No scans were excluded due to poor image quality

# 2.2 Preprocessing

To address domain shifts caused by variations in OCTA imaging devices, all input images were subjected to a standardized preprocessing pipeline. First, column-wise z-score normalization was applied, whereby each column of the image was normalized using its own mean and standard deviation [18]. This technique reduces directional intensity variation and enhances inter-device consistency. For multi-channel inputs (OCT and OCTA), this normalization was performed independently on each channel to preserve modality-specific contrast characteristics.

To further suppress background noise and enhance lesion visibility, a thresholding operation was applied following normalization. Specifically, pixel values below -0.5 were set to zero, effectively attenuating low-intensity artifacts and improving the signal-to-background ratio in regions affected by noise or motion-induced fluctuations.

# 2.3 Ground truth label generation

In this study, two types of ground truth labels were generated, each designed for a specific model task: VRI segmentation, and RNV diagnosis with membrane segmentation.

In this study, retinal specialists manually annotated the VRI boundary on each B-scan. Using these annotations, binary segmentation masks were generated by labeling pixels above the VRI as vitreous and those below as the retinal region.

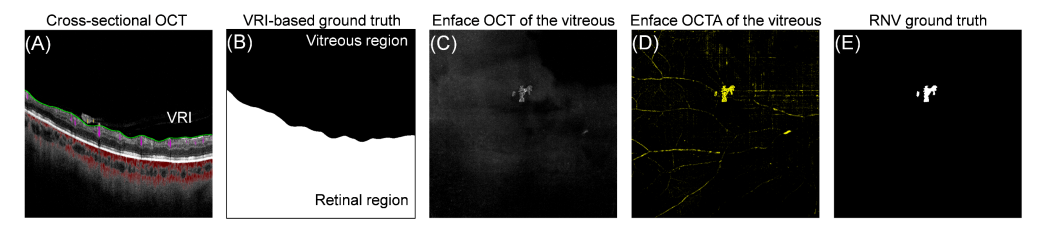


**Fig. 1.** Ground truth label generation workflow. (A) Cross-sectional OCT image showing expert-annotated VRI boundary with flow signal overlaid (yellow: RNV flow; violet: retinal flow; red: choroidal flow). (B) Binary VRI-based ground truth mask showing the vitreous (black) and retina (white). (C) *En face* OCT projection of the vitreous slab, used to identify candidate hyperreflective structures suggestive of RNV. (D) *En face* OCTA projection of the vitreous slab, used to delineate the final RNV boundaries. (E) Manually annotated RNV ground truth, The lesion locations were first identified on *en face* OCT images, and the membrane boundaries were delineated on *en face* OCTA based on the clearer flow-signal contrast between RNV and background. The enclosed regions were then filled to generate the final ground-truth mask.

En face projections of the vitreous slab were used to annotate RNV lesions. Based on these projections, retinal specialists manually annotated RNV as follows: first, hyperreflective structures located on en face OCT of the vitreous slab were identified as candidate lesions [19]; second, their boundaries were carefully delineated on en face OCTA images. The annotations generated from the en face OCTA image, where features such as tangled vasculature or abnormal sprouting patterns were identified, and subsequently verified on cross-sectional OCT

overlaid by OCTA (Fig. 1A). Each annotation was independently reviewed and confirmed by at least two retinal specialists (Fig. 1E).

## 2.4 Algorithm outline

The proposed algorithm incorporates two convolutional neural networks (CNNs): one for VRI segmentation and the other for *en face* RNV detection (Fig. 2). The VRI segmentation module serves as the foundation for subsequent RNV analysis by generating anatomically consistent *en face* OCTA and OCT projections.

Based on the predicted VRI, multiple anatomically relevant *en face* projection slabs are generated from both OCT and OCTA volumes. These projection slabs are subsequently fed into the RNV detection network. When RNV is present, the model produces a pixel-wise segmentation mask outlining the lesion area. The resulting detection map represented the predicted lesion region and was used for subsequent quantitative overlap and detection analyses. For visualization purposes, the flow signals confined to the predicted lesion area were extracted from *en face* OCTA of the vitreous slab and projected onto the corresponding *en face* OCTA of the inner slab. Otherwise, scans without detectable lesions are classified as non-RNV.

When visualizing vessels within RNV lesions, vessel masks were further refined using a multi-scale adaptive thresholding method combined with morphological constraints. This post-processing step enhances local contrast and selectively preserves vessel-like structures that overlap with the coarse membrane masks.

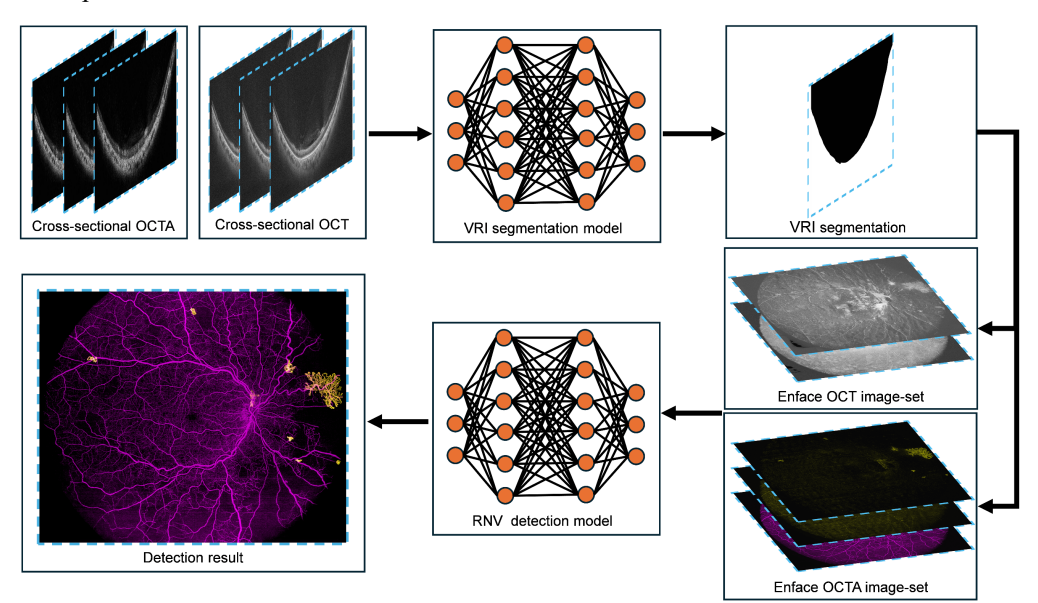


Fig. 2. Schematic overview of the proposed automated RNV identification and segmentation framework. The input consists of cross-sectional structural OCT and OCTA images, while the final output is a pixel-wise RNV segmentation map visualized on the *en face* OCTA projection of the vitreous slab onto the corresponding *en face* OCTA of the inner slab. Two separate CNNs are employed: the first segments the VRI boundary, which is then used to generate *en face* OCT and OCTA image sets; the second CNN detects and segments the RNV membrane based on these anatomically guided *en face* OCT and OCTA inputs.

#### 2.5 Deep learning model for VRI segmentation

To segment the VRI, we designed a deep learning model based on the U-Net architecture [20], which takes as input three consecutive B-scan frames, with each frame comprising paired structural OCT and OCTA frames. These six images are concatenated along the channel axis to form a 6-channel input tensor, enabling the model to leverage local volumetric context. This multi-frame, dual-modality configuration provides complementary structural and vascular

information, which is useful for robustly identifying the vitreous region and minimizing segmentation errors caused by noise or morphological variability (Fig. 3). The network outputs a binary segmentation mask, classifying each pixel as either in the vitreous region above the VRI or the retinal region below the VRI.

To optimize the VRI segmentation model we adopted a composite loss function that combines Binary Cross-Entropy (BCE) Loss [21] and Dice Loss, two widely used metrics in medical image segmentation tasks. BCE Loss ensures pixel-wise classification accuracy by penalizing incorrect predictions at the individual pixel level. In contrast, Dice Loss measures the spatial overlap between the predicted and ground truth regions, making it particularly effective for addressing class imbalance, which is common in anatomical boundary segmentation. The final loss function is formulated as a weighted sum of the two components to leverage their complementary strengths and achieve more robust and accurate VRI delineation:

$$\mathcal{L}_{BCE} = -\frac{1}{N} \sum_{i=1}^{N} (y_i \log(\hat{y}_i) + (1 - y_i) \log(1 - \hat{y}_i))$$
 (1)

$$\mathcal{L}_{Dice} = 1 - \frac{2\sum_{i=1}^{N} y_i \hat{y}_i + \epsilon}{\sum_{i=1}^{N} y_i + \sum_{i=1}^{N} \hat{y}_i + \epsilon}$$
 (2)

$$\mathcal{L}_{S} = \alpha \mathcal{L}_{BCE} + (1 - \alpha) \mathcal{L}_{Dice}$$
(3)

Here,  $y_i$  denotes the ground truth label of the *i*-th sample, and  $\hat{y}_i$  represents the corresponding predicted probability. N is the total number of samples in the dataset. A small constant  $\epsilon$  is added to both the numerator and denominator to avoid division by zero and ensure numerical stability during training.  $\mathcal{L}_S$  is defined as the final loss value used for training the VRI segmentation network, and  $\alpha$  is a weighting factor that balances the contributions of the BCE and Dice loss components, with its numerical value set to 0.5 in our experiments.

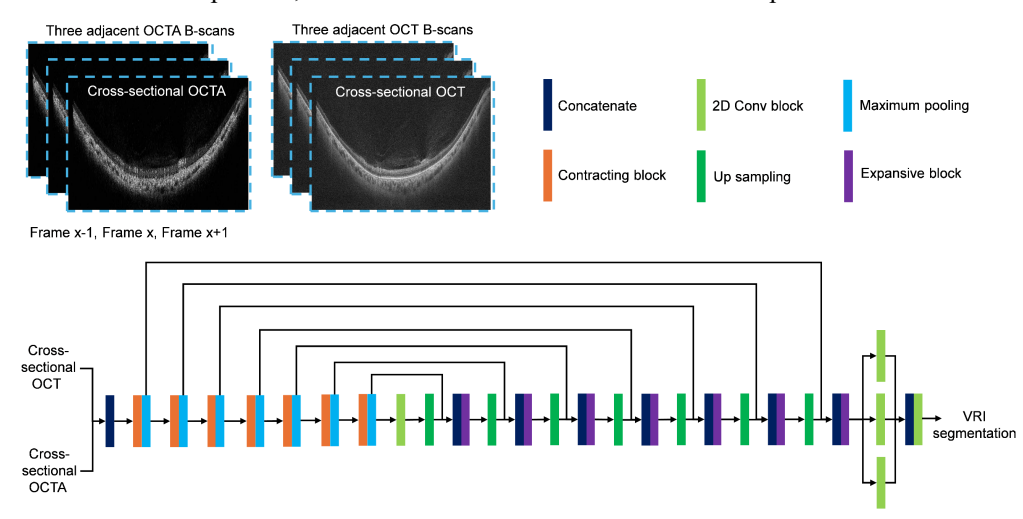


Fig. 3. Schematic CNN architecture for VRI boundary segmentation. The model inputs three adjacent OCT and OCTA B-scans to capture both structural and vascular features with local 3D context. Multi-scale feature fusion is applied using parallel  $1 \times 1$ ,  $3 \times 3$ , and  $5 \times 5$  convolutions, enabling accurate and robust VRI segmentation across varied retinal structures.

#### 2.6 Deep learning model for RNV diagnosis and segmentation

The next step, RNV segmentation, uses *en face* projections generated from both OCT and OCTA volumes based on the VRI segmentation using the maximum projection method [22]. By isolating the vitreous, this approach reduces segmentation artifacts from superficial vessels

and suppresses confounding signals. Specifically, five types of *en face* images were constructed as model inputs, each capturing complementary structural or vascular cues relevant to neovascular pathology and supporting accurate RNV diagnosis and membrane segmentation (Fig. 4).

## (1) en face OCT of the vitreous

The vitreous slab was defined using the VRI as the lower boundary and extended axially upward without a fixed height. This definition enables comprehensive coverage of neovascular structures in the vitreous that vary substantially in height and morphology. *En face* OCT projection of this slab highlights hyperreflective lesions in the vitreous that are strongly indicative of pathological neovascular proliferation.

## (2) en face OCTA of the vitreous

The *en face* OCTA projection of the same slab provides a detailed visualization of abnormal blood flow within the vitreous region, which is avascular in normal eyes.

## (3) en face OCT of GCC

The GCC slab was defined with the VRI as the upper boundary and extended 80 µm into the retina, corresponding to the typical thickness of the ganglion cell complex [23]. In advanced stages, RNV can exert mechanical traction or pressure on the inner retinal layers, resulting in localized compression or deformation that can offer important complementary useful for RNV detection [24].

## (4) en face OCTA of GCC

The *en face* OCTA projection of the GCC slab provides spatial priors of large superficial retinal vessels that can protrude slightly towards the VRI and elevate its contour. Combined with minor inaccuracies in VRI segmentation, this can produce segmentation artifacts appearing as flow in the vitreous. Incorporating the GCC-layer OCTA into the model input enables the network to recognize and discount such artifacts based on their spatial distribution patterns.

#### (5) subtracted en face OCTA

The subtracted *en face* OCTA image of the vitreous was generated by subtracting a scaled version of the GCC-layer OCTA signal from the vitreous OCTA image. This subtraction enhances the contrast of neovascular tufts by reducing artifacts from superficial vasculature caused by segmentation inaccuracies, as demonstrated in previous work on OCTA image enhancement [25, 26].

To preserve modality-specific features, a dual-branch encoding design was adopted, allowing OCT and OCTA inputs to be processed separately during early feature extraction.

To enhance detection sensitivity and structural fidelity, several architectural modifications were integrated into the U-Net backbone. Squeeze-and-excitation (SE) blocks are inserted after each encoder and decoder stage to recalibrate channel responses [27], improving the model's ability to detect small or low-contrast neovascular tufts. In addition, depthwise separable convolutions replace standard convolutions in the second layer of each block [28], reducing computational complexity while preserving discriminative power. Multi-scale fusion and skip connections are used to support both high-resolution localization and contextual understanding.

To address the inherent class imbalance in RNV segmentation, where the neovascular regions (foreground) occupy only a small portion of the image compared to the large background, we adopted a loss function that explicitly separates and balances the contributions of both foreground and background. Specifically, we compute Mean Squared Error (MSE) losses independently for the foreground and background, then take their average as the final loss:

$$\mathcal{L}_D = \frac{\omega_b}{N_b + \epsilon} \sum_{i}^{\mathbb{I}_{b,i}} (y_i - \hat{y}_i)^2 + \frac{\omega_f}{N_f + \epsilon} \sum_{i}^{\mathbb{I}_{f,i}} (y_i - \hat{y}_i)^2$$
 (4)

 $\mathcal{L}_D$  is defined as the final loss value used for training the RNV membrane segmentation network. In this formulation,  $\mathbb{I}_{b,i}$  and  $\mathbb{I}_{f,i}$  are indicator functions that select background and foreground pixels respectively;  $N_b$  and  $N_f$  the total number of background and foreground pixels; and  $\epsilon$  is a small constant to avoid division by zero, and  $\omega_b$ ,  $\omega_f$  are weighting factors for background and foreground losses, respectively, set to 0.4 and 0.6. This formulation helps the model better capture neovascular regions despite their small size in the image.

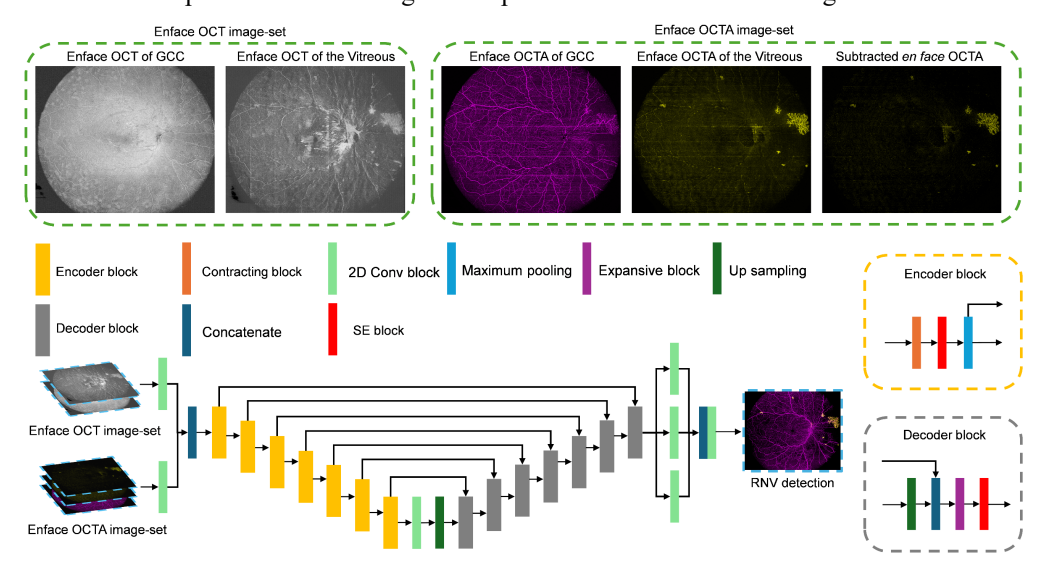


Fig. 4. Overview of the dual-branch CNN for RNV membrane detection. En face OCT and OCTA image sets are processed through independent encoder branches. Each encoder block integrates standard and depthwise convolutions, squeeze-and-excitation (SE) attention, and pooling. Decoder blocks include up sampling, skip connections, and SE recalibration. A multi-scale fusion head generates the final segmentation.

## 2.7 Training and evaluation

To enhance the robustness and generalization ability of the model, data augmentation was applied to 50% of the samples in each training batch. Two augmentation strategies were employed: (1) brightness adjustment, in which image intensities were randomly scaled to simulate varying illumination conditions; and (2) independent Gaussian noise applied along image columns (mean = 0, standard deviation = 0.1) to simulate acquisition noise and scanning artifacts commonly observed in OCT/OCTA imaging. These augmentations were applied to both structural OCT and OCTA inputs.

To ensure unbiased evaluation, scans from the same eye were never included in both training and testing sets, thereby eliminating any overlap between sets. The data were randomly divided, with approximately 70% allocated for training and 30% for testing. The network was implemented in PyTorch and trained on an NVIDIA RTX 4090 GPU with CUDA 11.8. We optimized the model using the Adam optimizer with a learning rate of  $1 \times 10^{-4}$  and applied early stopping based on validation Dice loss with a patience of 20 epochs to prevent overfitting. Training was conducted for a maximum of 1000 epochs with a batch size of 2, and model weights were initialized with a ReLU-specific variance scaling method to stable training [29].

#### 3. Results

#### 3.1 Dataset composition

In total, 476 scans (including repeat and follow-up sessions) were collected from the Solix (Visionix/Optovue) device across different retinal regions. An additional 85 scans were

collected from the DREAM OCT (Intalight) device, and 28 independent scans without repeat imaging were collected from the S1-OCTA (Canon) device (Table 1).

Table 1. Distribution of RNV and Non-RNV Cases Across Devices and Scan Sizes

Device	Scan Size (mm)	Training (Eyes/Scans)		Testing (Eyes/Scans)	
		RNV	Non-RNV	RNV	Non-RNV
Solix	9 × 9*	30/168	31/181	18/50	21/77
DREAM OCT	26 × 21	43/56	7/7	18/19	3/3
S1-OCTA	23 × 20	18/18	1/1	8/8	1/1

<sup>\*</sup>Solix widefield image (17  $\times$  17 mm) obtained by montage of four 9  $\times$  9 mm scans.

## 3.2 VRI segmentation

To evaluate VRI segmentation accuracy, we selected B-scans containing RNV regions from each subject. Two graders independently delineated the VRI boundary using our customized COOL-ART software [30] and the final reference standard was obtained by averaging their annotations. The absolute error of the model-predicted boundary was then computed with respect to this reference, reported as mean  $\pm$  standard deviation (in pixels). This pixel-wise boundary error analysis provides a direct and anatomically meaningful assessment of segmentation performance (Table 2).

Table 2. Performance of VRI Segmentation on Different Devices

Device	Resolution (µm/pixels)	Segmentation Error (Mean ± std, pixels)	
Solix	3.05	$0.65\pm1.51$	
DREAM OCT	2.00	$1.32\pm3.15$	
S1-OCTA	4.00	$2.13 \pm 4.77$	

In addition to the quantitative evaluation reported in Table 2, we further assess the qualitative performance of our VRI segmentation algorithm using three representative OCTA cases exhibiting distinct RNV morphologies. RNV is commonly presented in three morphological types: tabletop, forward, and flat. Flat-type RNV lies tightly adherent to the VRI, making it difficult to distinguish the boundary between pathological and normal tissue (Fig. 5 Row 1). The other two types separate further from the VRI, making the segmentation task easier, although the algorithm still must learn the features associated with each. Our approach is capable of dealing with each type (Fig. 5).

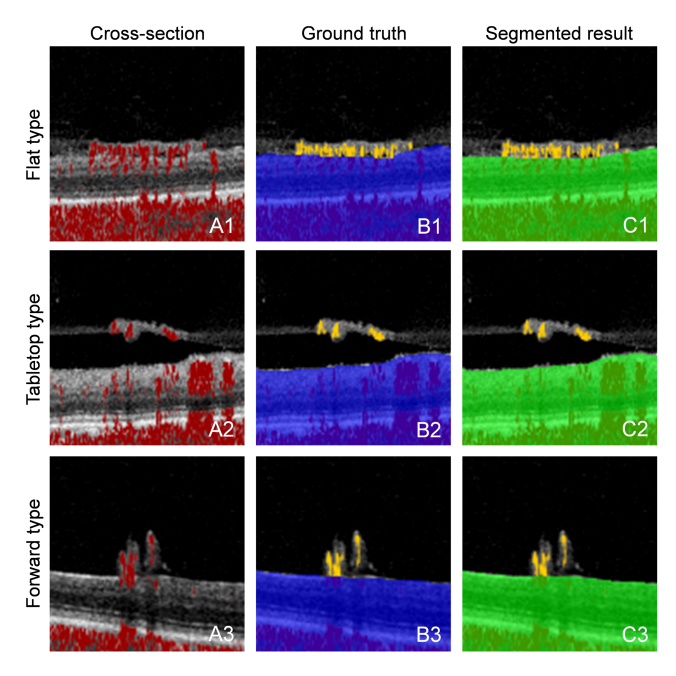


**Fig. 5.** Qualitative evaluation of VRI segmentation performance across three representative RNV morphologies: flat type, tabletop type, and forward type. Each row (A1-C1, A2-C2, A3-C3) includes three columns. (A) Original cross-sectional OCT image with all flow signals shown in red (prior to VRI segmentation). (B) Manually annotated ground truth with flow signals color-coded according to VRI position, red for normal retinal vasculature (including inner retinal and choroidal vessels), and yellow for RNV located in the vitreous. (C) Segmented result region with the same color scheme. (Row 1) Flat type. (Row 2): Tabletop type. (Row 3): Forward type. In each case, although the RNV morphologies varied substantially, the VRI segmentation agreed with grader annotations.

## 3.3 RNV diagnosis and segmentation

#### 3.3.1 Quantitative evaluation

The performance of RNV diagnosis was evaluated at the case level, where the presence of any neovascular lesion within an eye was considered indicative of a positive diagnosis. The model was assessed based on its ability to correctly identify the presence of each lesion. In contrast, segmentation performance was evaluated at the pixel level by comparing the predicted lesion masks to the manual annotations using IOU and F1 Score.

$$Precision = \frac{TP}{TP + FP}$$
 (5)

$$Recall = \frac{TP}{TP + FN}$$
 (6)

$$F1 = 2 \times \frac{\text{Precision} \times \text{Recall}}{\text{Precision} + \text{Recall}}$$
 (7)

$$IOU = \frac{GT \cap Out}{GT \cup Out}$$
 (8)

Here proposed algorithm. TP, FP, and FN refer to the numbers of true positives, false positives, and false negatives, respectively. The proposed algorithm achieved high performance in both diagnostic (AUC and sensitivity) and segmentation (IOU and F1-score) tasks (Table 3).

Table 3. Performance of RNV Diagnosis and Membrane Segmentation on Different Devices

	RNV Diagnosis		RNV Segmentation	
Device	AUC	Sensitivity	F1 Score	IOU
Solix	0.99	0.92	0.92±0.20	0.88±0.22
DREAM OCT	0.98	0.82	$0.90\pm0.25$	$0.87 \pm 0.27$
S1-OCTA	0.96	0.76	$0.79\pm0.35$	$0.76\pm0.37$

#### 3.3.2 Performance demonstrated on three devices

To further illustrate its robustness across different imaging conditions, we highlight representative examples from the three OCTA devices. The Solix (Visionix/Optovue) device provides the highest image resolution among the three imaging systems, enabling clear visualization of *en face* OCTA projections (Fig. 6 row 1). Although prominent superficial vessel signals are visible in the vitreous, the proposed algorithm accurately distinguishes true RNV lesions from these overlying vessels. The DREAM OCT (Intalight) device, with its ultrawide scanning area of  $26 \times 21$ -mm, enables visualization of large-scale RNV lesions (Fig. 6 row 2). Despite the extensive membrane area in this example, the algorithm successfully captures the full extent of the lesion, allowing for reliable computation of lesion-level quantitative metrics. The S1-OCTA (Canon) device also offers a wide field of view (Fig. 6 row 3).

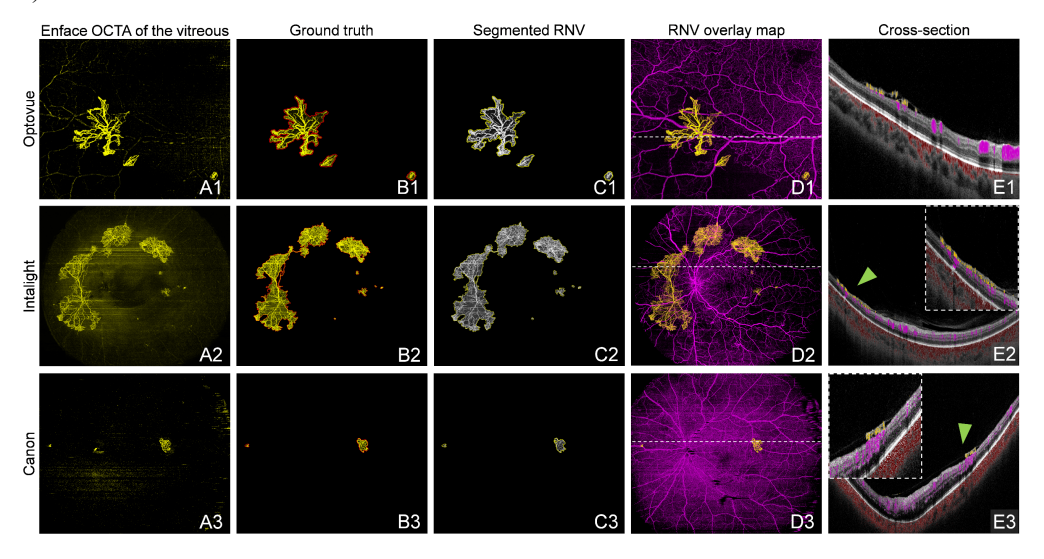


Fig. 6. Visualization of RNV segmentation results from three representative cases acquired using different OCTA devices. Each row corresponds to one device: (Row 1): Solix (Visionix/Optovue), (Row 2): DREAM OCT (Intalight), and (Row 3): S1-OCTA (Canon). (A) En face OCTA projection of the vitreous. (B) Manually annotated OCTA-based ground truth, with the lesion area visualized on en face OCTA projection of the vitreous slab. (C) Segmentation results predicted by the proposed algorithm. (D) Segmented RNV overlaid on the original inner en face OCTA image. (E) Structural OCT cross-section at the location of the white line in (D), with flow signal overlaid (yellow: RNV flow signals; violet: normal inner retinal vasculature; red: choroidal flow), including blow-up views to highlight the RNV region indicated by the green arrow. The proposed algorithm was able to successfully segment RNV across these three cases from different devices.

#### 3.3.3 Performance on clinically challenging conditions

Retinal hemorrhage can sometimes appear as intensely hyperreflective regions on *en face* OCT and may even present with faint OCTA signals, which can lead to misinterpretation as RNV due to their similar structural and blood-flow signal resemblance. These hemorrhagic areas

exhibit bright signals on *en face* OCT but lack the well-defined flow patterns characteristic of neovascular lesions (Fig. 7). By jointly leveraging structural and vascular information, the proposed algorithm successfully distinguishes hemorrhage from true RNV, demonstrating robustness in complex pathological scenarios.

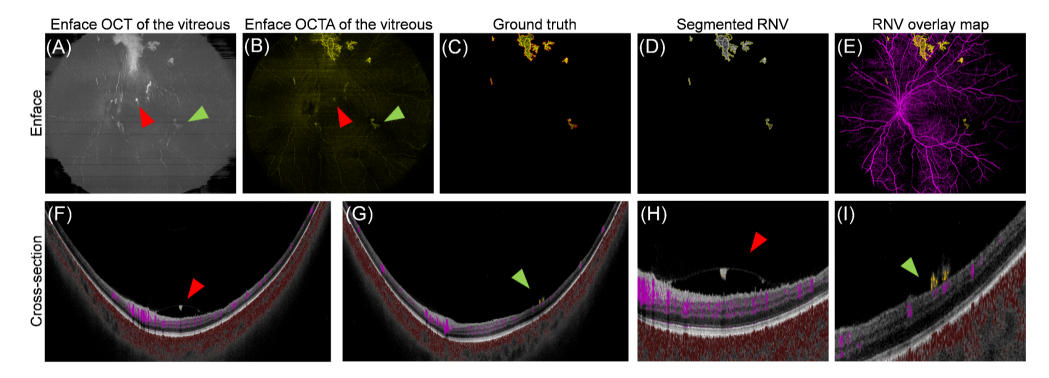


Fig. 7. Visualization of RNV segmentation results from a case with hemorrhage acquired using the DREAM OCT (Intalight) device. Throughout, red arrows indicate the location of the hemorrhage age, while green indicates the RNV lesion. (A) En face OCT and (B) OCTA projection of the vitreous using the VRI segmentation result. (C) Manually annotated RNV ground truth, with the lesion area visualized on en face OCTA projection of the vitreous slab. (D) Predicted segmentation results by the proposed algorithm. (E) Overlay of segmented RNV on the original en face OCTA image. (F-I) Structural OCT cross-sectional images with flow signal overlaid (yellow: RNV; violet: retinal; red: choroidal) can help verify algorithm output. (F) Structural OCT B-scan at the hemorrhage site. (G) Structural OCT B-scan at the RNV site. (H) Magnified view of panel F. (I) Magnified view of panel G. The same color scheme applies to all cross-sectional panels (F-I).

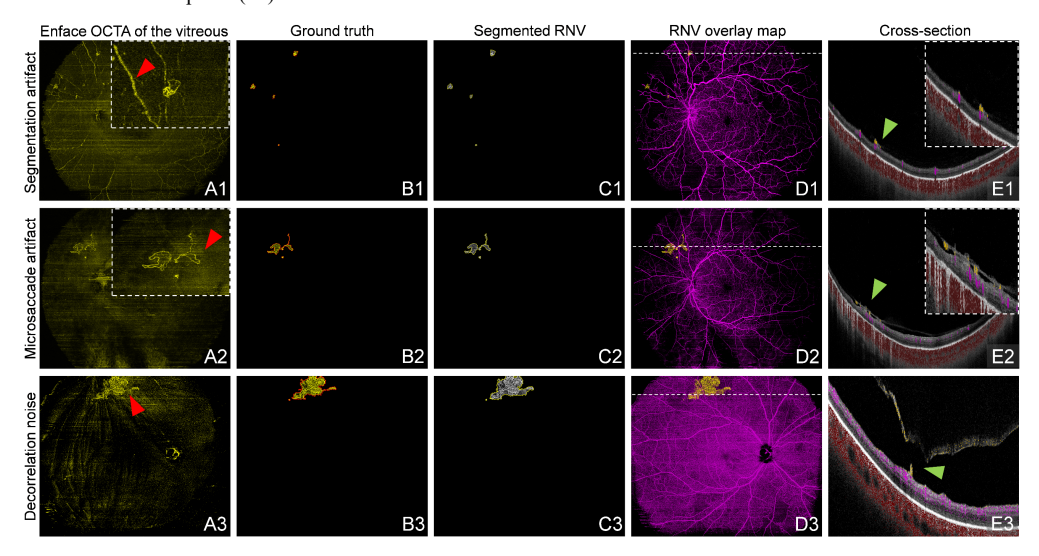


Fig. 8. Visualization of RNV segmentation results on low-quality scans from two different devices. (A) En face OCTA projection of the vitreous. Red arrows indicate the location of the artifact. (B) Manually annotated RNV ground truth from en face OCTA, with the lesion area visualized on en face OCTA projection of the vitreous slab. (C) Segmentation results predicted by the proposed algorithm. (D) Overlay of segmented RNV on the original inner en face OCTA image. (E) Structural OCT cross-section at the location of the white line in (D), with flow signal overlaid, where yellow indicates RNV flow, violet represents normal retinal vasculature, and red denotes choroidal flow, with blow-up views provided to highlight the RNV region in (E1). Green arrows indicate the location of the RNV lesion. (Row 1): a scan from an Intalight DREAM OCT device showing segmentation artifacts from large superficial vessels. (Row 2): a scan from an Intalight DREAM OCT device with microsaccade artifacts. (Row 3): a scan from a Canon S1-OCT device exhibiting pronounced decorrelation noise. In all three cases, the algorithm still obtained a results similar to the ground truth.

## 3.3.4 Performance on challenging scans

Reliable *en face* OCTA projections for RNV analysis are challenged by several types of artifacts (Fig. 8). One of the most problematic artifacts are segmentation artifacts originating from large superficial retinal vessels, which can induce protrusions of the VRI surface. These protrusions often lead to segmentation errors, causing normal retinal vessels to be misclassified as pathological flow. Additional artifacts such as microsaccade artifacts, bulk motion distortion, and decorrelation noise further complicate image interpretation and hinder accurate lesion segmentation [31].

The robustness of the proposed algorithm under suboptimal imaging conditions was evaluated using representative low-quality cases from different devices (Fig. 8). In the DREAM OCT (Intalight) case (Fig. 8 row 1), protrusions of the VRI surface led to segmentation errors that projected superficial vessels into the vitreous slab, creating false-positive signals that affected RNV detection. In another Intalight case (Fig. 8 row 2), weak flow signals and imaging artifacts make it challenging to delineate the RNV membrane even for experienced human graders, yet the algorithm successfully identified the lesion. Similarly, in the S1-OCTA (Canon) case (Fig. 8 row 3), elevated decorrelation noise contributed to reduced image contrast and ambiguous boundaries posed difficulties for both graders and the model, contributing to the lower IOU scores observed on this device. Despite these limitations, the algorithm was still able to localize the RNV membrane, demonstrating reliable performance even under poor image quality.

# 3.3.5 Performance for visualizing ill-defined lesions on fluorescein angiography

Fluorescein angiography (FA) continues to be a standard clinical procedure for assessing RNV. However, not all RNV lesions that can be identified with OCT and OCTA are captured by FA [9, 32]. Lesions that remain unidentified by FA are often small, meaning that these features could pose a problem for image graders reviewing OCT and OCTA data in high throughput scenarios. We were able to identify cases in which lesions do not appear in FA but were nonetheless correctly segmented using our approach (Fig. 9)

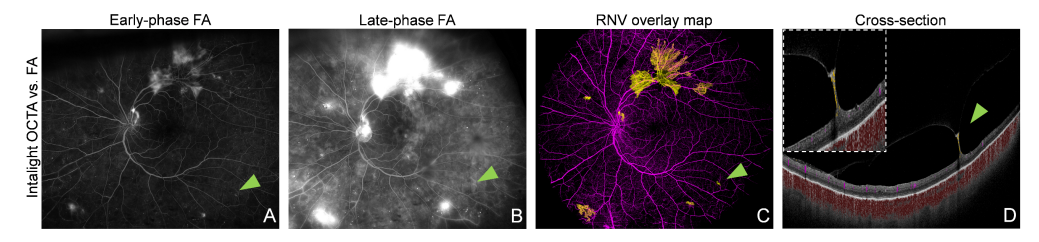


Fig. 9. Comparison of RNV detection results between FA and OCTA acquired using the DREAM OCT (Intalight) device. Throughout, green arrows indicate the location of the RNV lesion. (A) Early-phase FA image showing hyperfluorescent neovascular lesions. (B) Late-phase FA image showing leakage from neovascular complexes. (C) Overlay of segmented RNV on the original inner *en face* OCTA image. (D) Structural OCT B-scan at the location of the green arrow in (C) showing flow signals (yellow: RNV flow; violet: inner retinal vasculature; red: choroidal flow), with blow-up views provided to highlight the RNV region.

## 3.3.6 Performance on smaller and larger fields of view

Clinical observations indicate that a substantial proportion of RNV lesions occur in peripheral retinal regions [33]. Consequently, detection frameworks limited to small fields of view may fail to capture the full spatial extent of RNV membranes or entirely miss peripheral lesions, underscoring the necessity of wide-field analysis. A notable limitation is the fixed 9 × 9-mm field of view of the Solix (Visionix/Optovue) device, which restricts the detectable area in OCTA scans. Such constraints often necessitate additional techniques such as image montage to improve field of view and the accuracy of progression tracking (Fig. 10 row 1). In contrast,

the DREAM OCT (Intalight) image of the same case (Fig. 10 row 2) demonstrates how a wider scanning area enables full delineation of the RNV membrane, thereby improving the reliability of longitudinal assessments. Our algorithm generalizes well to wide-field OCTA data effectively segments RNV in both of these fields of view.

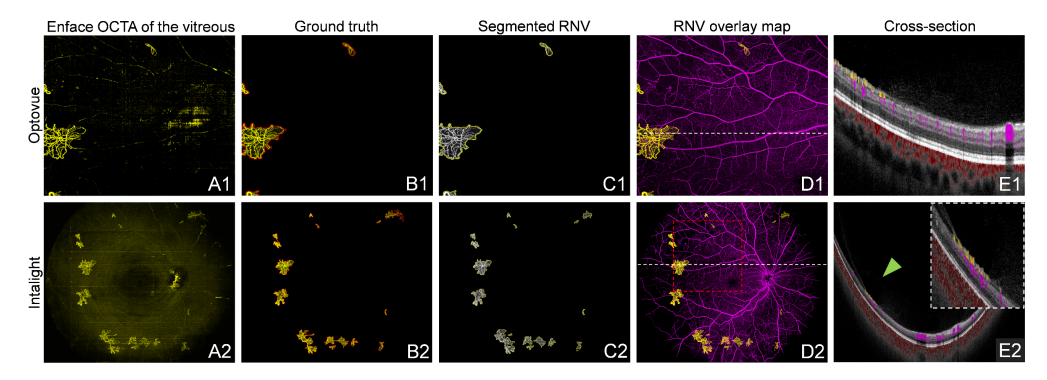
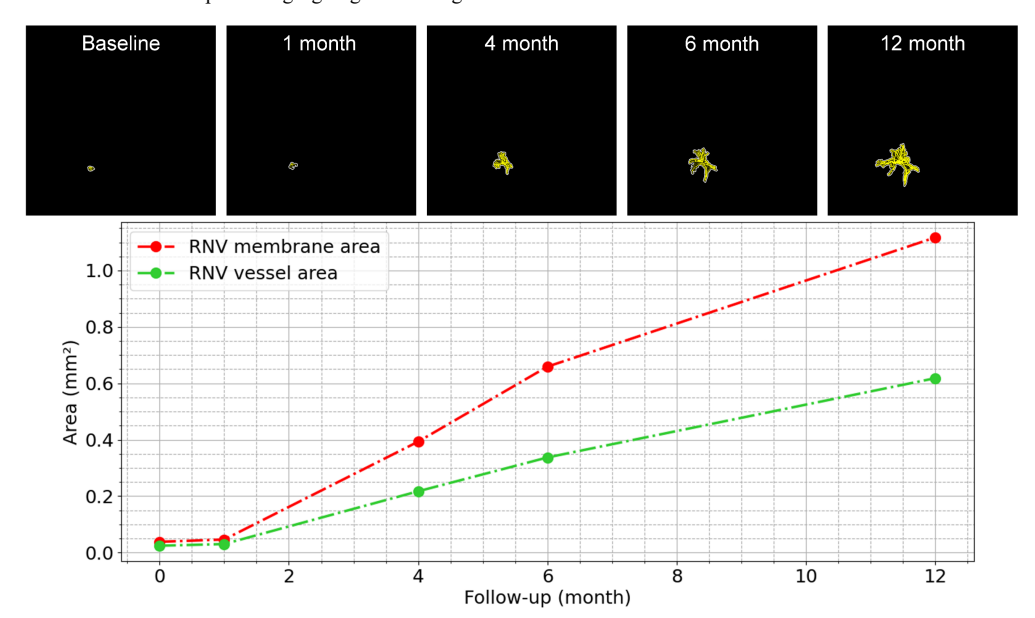


Fig. 10. Visualization of RNV segmentation results from a representative case imaged using two different devices. The first row corresponds to the Solix (Visionix/Optovue) device, and the second row to the DREAM OCT (Intalight) device. (A) Enface OCTA projection of the vitreous. (B) Manually annotated RNV ground truth on OCTA, with the lesion area visualized on en face OCTA projection of the vitreous slab. (C) Segmentation results predicted by the proposed algorithm. (D) Overlay of segmented RNV on the original inner en face OCTA image. The red dashed box indicates the region corresponding to the Solix device. (E) Structural OCT cross-section at the location of the white line in (D), showing overlaid flow signals, where yellow indicates RNV flow, violet represents normal inner retinal vasculature, and red denotes choroidal flow, with blow-up views highlighting the RNV region. Green arrows indicate the location of the RNV lesion.



**Fig. 11.** Longitudinal segmentation of RNV membranes in a DR patient over 12 months without any treatment intervention. Each panel shows the segmented RNV region at a specific timepoint: Baseline, 1 month, 4 months, 6 months, and 12 months. Yellow regions denote the refined RNV vessel mask, and white outlines indicate the segmented membrane boundary. These visualizations support temporal tracking of lesion growth and vascular remodeling.

## 3.3.7 Longitudinal monitoring

In addition to detecting RNV lesions, our method supports precise morphological measurements critical for disease monitoring. We applied it to segment RNV membrane areas

on  $9 \times 9$ -mm OCTA scans from a DR patient with 12 months of longitudinal follow-up. The resulting refined masks enable reliable quantification of neovascular progression, including changes in lesion area and vascular density over time (Fig. 11).

#### 4. Discussion and conclusion

In this study, we developed a fully automated deep learning framework for the identification and segmentation of RNV in widefield OCT/OCTA data volumes. This framework achieved two primary tasks: (1) diagnosis of RNV, and (2) segmentation of the RNV lesion in *en face* images. The proposed method was evaluated on datasets from two clinics and three different commercial OCTA devices, with no exclusions for poor image quality. Our validation results indicate that our approach is accurate on a clinically realistic dataset. In particular, this work represents an RNV detection approach valid for widefield OCT and OCTA data, which could offer an advantage in clinical practice relative to existing approaches that operate on conventional (smaller) fields of view. This performance required several innovations, as indicated below.

First, our approach relied on a novel supporting network that supplied VRI segmentation. Previous studies have commonly employed the VRI slab to detect RNV [13, 34], as it captures extraretinal lesions that extend into the vitreous. However, the effectiveness of this approach is limited by the accuracy of automated segmentation of both the VRI and posterior vitreous membrane. Posterior vitreous membrane segmentation methods often use fixed-height columns to approximate membrane location [14], which can fail to capture the full extent of RNV lesions. Furthermore, previously published VRI segmentation results have been reported to suffer performance decline when assessing flat-type RNV cases [35]. Consequently, in such methods manual correction may be required for accurate detection in such approaches. Our approach addresses this difficulty by introducing two task-specific supporting slabs: a vitreous slab above and a retinal slab below the VRI. Unlike conventional multi-layer retinal segmentation frameworks [36], we reformulate VRI segmentation as a binary localization task. This not only simplifies the model design but also enhances robustness across devices and field curvatures. Notably, the model performs reliably even when neovascular tissue is closely adherent to the VRI. And, since we do not use fixed height columns, we do not risk neovascular vessels extending upward beyond the region of interest defined by such columns. This anatomically informed strategy enables consistent delineation of RNV membranes with irregular morphology or variable height.

Another issue that can deleteriously affect RNV segmentation is the presence of normal large superficial vessels. Segmentation artifacts from large superficial retinal vessels can mimic or obscure true RNV signals in the vitreous, leading to false positives and complicating automated analysis. On *en face* projections, these vessels often produce VRI protrusions that resemble neovascular tufts. These features are particularly challenging to distinguish from true pathology without anatomical context. To address this, we incorporated additional imaging inputs: *en face* OCTA projections of the GCC slab as spatial priors for superficial vasculature, and a vessel-suppressed vitreous OCTA image obtained by subtracting scaled GCC flow signal from the vitreous slab. This strategy, validated in prior studies [25], effectively suppresses segmentation artifacts and enhances the visibility of neovascular tufts, thereby improving the specificity and robustness of RNV detection.

Other studies have also leveraged anatomical cues for neovascular detection. Wang et al [37]. Developed a deep learning system for optic disc neovascularization (NVD) using 6 × 6-mm en face OCTA scans that first segments the optic disc boundary to guide the NVD detection, achieving strong diagnostic performance within a limited field of view. In contrast, some approaches omit VRI segmentation and instead rely on vessel-derived features. For instance, Tun et al. [12] proposed a feature-based method that computes vessel density, bifurcation density, and vessel thinness from en face OCTA scans (12 × 12-mm field of view)

acquired using a swept-source system, followed by SVM-based RNV localization. While effective for coarse localization, such methods are constrained by the scan size and struggle with precise boundary delineation in cases of heterogeneous lesion morphologies or noisy signals, and they lack the capacity for detailed lesion analysis. By contrast, our approach incorporates VRI segmentation as a structural prior, providing reliable anatomical for RNV segmentation across widefield retinal images.

Due to these technical considerations our method was successful in diagnosing and segmenting RNV in widefield OCT/OCTA. The transition from conventional fields of view to widefield OCT/OCTA has important clinical consequences, particularly in screening for pathologic features that could be found throughout the retina. RNV itself is an example of such a pathology, and in fact it may be more prevalent in the periphery, outside the field of view of macula-centered conventional OCT/OCTA. However, alternative screening approaches like widefield color fundus photography may not provide detection sensitivity commensurate with that provided by OCT/OCTA. Widefield OCT/OCTA combines high detection sensitivity with expansive coverage of the retina. In combination, OCT/OCTA imaging and automated RNV detection as described in this study could provide an improved means of diagnosing RNV. Our approach is also able to assess RNV longitudinal dynamics (Fig. 11), which could provide indications for treatment interventions. In total, we believe that our results demonstrate automated RNV analysis in widefield OCT/OCTA is a promising avenue for ophthalmic translational research.

This study has several limitations. First, the dataset size remains relatively small, which may limit the generalizability of the model to broader populations. Second, RNV lesions with blurred or ambiguous boundaries, especially those closely apposed to the VRI, remain difficult to segment accurately. These cases are inherently challenging, even for experienced human graders. Finally, while the proposed method demonstrates robust performance across most RNV morphologies, segmentation may fail in regions where the VRI is significantly distorted or elevated, or where it is torn, often due to traction exerted by adjacent neovascular tissue. In such cases, manual correction may be required to ensure accurate membrane delineation.

In future work, we plan to expand the dataset scale and diversity and explore the integration of multimodal clinical data such as FA and patient records to provide richer diagnostic context. To further alleviate annotation burdens, we also aim to incorporate semi-supervised or unsupervised learning strategies for VRI and RNV segmentation. These approaches could leverage large quantities of unlabeled OCTA data to improve model robustness while reducing dependence on expert-annotated ground truth. Additionally, we will continue refining the model architecture to achieve more accurate delineation of complex neovascular patterns, thereby facilitating broader clinical adoption and real-world scalability.

**Funding.** National Institutes of Health (R01 EY 036429, R01 EY035410, R01 EY024544, R01 EY027833, R01 EY031394, R43EY036781, P30 EY010572, T32 EY023211, UL1TR002369); the Jennie P. Weeks Endowed Fund; the Malcolm M. Marquis, MD Endowed Fund for Innovation; Unrestricted Departmental Funding Grant and Dr. H. James and Carole Free Catalyst Award from Research to Prevent Blindness (New York, NY); Edward N. & Della L. Thome Memorial Foundation Award, and the Bright Focus Foundation (G2020168, M20230081).

**Disclosures.** Yali Jia: Optovue/Visionix (P, R), Genentech/Roche (P, R, F), Ifocus Imaging (I, P), Optos (P), Boeringer Ingelheim (C), Kugler (R); Tristan.T. Hormel: Ifocus Imaging (I); Jie Wang: Optovue/Visionix (P, R), Genentech/Roche (P, R), Ifocus Imaging (I, P); Yukun Guo: Optovue/Visionix (P), Genentech/Roche (P, R); Ifocus Imaging (P); Steven T. Bailey: Optovue/Visionix (F); Kotaro Tsuboi: Alcon Japan (F); Thomas S. Hwang: None; Jennifer K. Sun, Novartis (F), Genentech/Roche (F), Novo Nordisk (F, R), Optovue/Visionix (F), Boehringer Ingelheim (F, R), Physical Sciences (F), Alcon (F)

**Data Availability.** The data sets generated and analyzed in this study are not publicly available at this time but may be obtained from the authors upon reasonable request.

#### References

- 1. N. Cheung, P. Mitchell, and T. Y. Wong, "Diabetic retinopathy," Lancet 376, 124-136 (2010).
- G. S. Tan, N. Cheung, R. Simó, et al., "Diabetic macular oedema," The lancet Diabetes & endocrinology 5, 143-155 (2017).
- J. W. Yau, S. L. Rogers, R. Kawasaki, et al., "Global prevalence and major risk factors of diabetic retinopathy," Diabetes care 35, 556-564 (2012).
- H. Khalid, R. Schwartz, L. Nicholson, et al., "Widefield optical coherence tomography angiography for early detection and objective evaluation of proliferative diabetic retinopathy," British Journal of Ophthalmology 105, 118-123 (2021).
- T. Y. Wong, J. Sun, R. Kawasaki, et al., "Guidelines on diabetic eye care: the international council of ophthalmology recommendations for screening, follow-up, referral, and treatment based on resource settings," Ophthalmology 125, 1608-1622 (2018).
- C. S. Lee, A. Y. Lee, D. A. Sim, et al., "Reevaluating the definition of intraretinal microvascular abnormalities and neovascularization elsewhere in diabetic retinopathy using optical coherence tomography and fluorescein angiography," American journal of ophthalmology 159, 101-110. e101 (2015).
- Y. Jia, S. T. Bailey, T. S. Hwang, et al., "Quantitative optical coherence tomography angiography of vascular abnormalities in the living human eye," Proceedings of the National Academy of Sciences 112, E2395-E2402 (2015).
- 8. Y. Jia, O. Tan, J. Tokayer, et al., "Split-spectrum amplitude-decorrelation angiography with optical coherence tomography," Optics express 20, 4710-4725 (2012).
- 9. K. Tsuboi, M. Mazloumi, Y. Guo, et al., "Early sign of retinal neovascularization evolution in diabetic retinopathy: a longitudinal OCT angiography study," Ophthalmology Science 4, 100382 (2024).
- 10. Y. Li, R. Zeghlache, I. Brahim, et al., "Segmentation, classification, and quality assessment of UW-octa images for the diagnosis of diabetic retinopathy," in MICCAI Challenge on Mitosis Domain Generalization (Springer, 2022), pp. 146-160.
- 11. Y. Guo, A. Camino, J. Wang, et al., "MEDnet, a neural network for automated detection of avascular area in OCT angiography," Biomedical optics express 9, 5147-5158 (2018).
- 12. Y. Z. Tun and P. Aimmanee, "Machine Learning-Based Retinal Neovascularization Localization in En face Optical Coherence Tomography Angiography Images Using Vessel Features," IEEE Access (2024).
- 13. T. Hirano, K. Hoshiyama, K. Hirabayashi, et al., "Vitreoretinal interface slab in OCT angiography for detecting diabetic retinal neovascularization," Ophthalmology Retina 4, 588-594 (2020).
- 14. E. H. Motulsky, G. Liu, Y. Shi, et al., "Widefield swept-source optical coherence tomography angiography of proliferative diabetic retinopathy," Ophthalmic Surgery, Lasers and Imaging Retina 50, 474-484 (2019).
- J. Wang, T. T. Hormel, S. T. Bailey, et al., "Signal attenuation-compensated projection-resolved OCT angiography," Biomedical Optics Express 14, 2040-2054 (2023).
- T. T. Hormel, D. Huang, and Y. Jia, "Advances in OCT angiography," Translational Vision Science & Technology 14, 6-6 (2025).
- 17. M. Hamada, K. Hirai, T. Wakabayashi, et al., "Practical Utility of Widefield OCT Angiography to Detect Retinal Neovascularization in Eyes with Proliferative Diabetic Retinopathy," Ophthalmology Retina 8, 481-489 (2024).
- 18. J. Wang, T. T. Hormel, Q. You, et al., "Robust non-perfusion area detection in three retinal plexuses using convolutional neural network in OCT angiography," Biomedical Optics Express 11, 330-345 (2019).
- 19. J. Huemer, H. Khalid, S. K. Wagner, et al., "Phenotyping of retinal neovascularization in ischemic retinal vein occlusion using wide field OCT angiography," Eye 35, 2812-2819 (2021).
- 20. O. Ronneberger, P. Fischer, and T. Brox, "U-net: Convolutional networks for biomedical image segmentation," in Medical image computing and computer-assisted intervention–MICCAI 2015: 18th international conference, Munich, Germany, October 5-9, 2015, proceedings, part III 18, (Springer, 2015), 234-241.
- U. Ruby and V. Yendapalli, "Binary cross entropy with deep learning technique for image classification," Int. J. Adv. Trends Comput. Sci. Eng 9(2020).
- T. T. Hormel, J. Wang, S. T. Bailey, et al., "Maximum value projection produces better en face OCT angiograms than mean value projection," Biomedical optics express 9, 6412-6424 (2018).
- 23. E. Yenice, A. Şengün, G. Soyugelen Demirok, et al., "Ganglion cell complex thickness in nonexudative agerelated macular degeneration," Eye 29, 1076-1080 (2015).
- 24. A. Ishibazawa, T. Nagaoka, A. Takahashi, et al., "Optical coherence tomography angiography in diabetic retinopathy: a prospective pilot study," American journal of ophthalmology 160, 35-44. e31 (2015).
- 25. J. Wang, T. T. Hormel, K. Tsuboi, et al., "Deep learning for diagnosing and segmenting choroidal neovascularization in OCT angiography in a large real-world data set," Translational Vision Science & Technology 12, 15-15 (2023).
- Y. Jia, S. T. Bailey, D. J. Wilson, et al., "Quantitative optical coherence tomography angiography of choroidal neovascularization in age-related macular degeneration," Ophthalmology 121, 1435-1444 (2014).
- J. Hu, L. Shen, and G. Sun, "Squeeze-and-excitation networks," in Proceedings of the IEEE conference on computer vision and pattern recognition, 2018), 7132-7141.
- 28. F. Chollet, "Xception: Deep learning with depthwise separable convolutions," in *Proceedings of the IEEE conference on computer vision and pattern recognition*, 2017), 1251-1258.
- K. He, X. Zhang, S. Ren, et al., "Delving deep into rectifiers: Surpassing human-level performance on imagenet classification," in *Proceedings of the IEEE international conference on computer vision*, 2015), 1026-1034.

- 30. M. Zhang, J. Wang, A. D. Pechauer, et al., "Advanced image processing for optical coherence tomographic angiography of macular diseases," Biomedical optics express 6, 4661-4675 (2015).
- 31. T. T. Hormel, D. Huang, and Y. Jia, "Artifacts and artifact removal in optical coherence tomographic angiography," Quantitative Imaging in Medicine and Surgery 11, 1120 (2021).
- 32. K. Tsuboi, M. Mazloumi, Y. Guo, et al., "Utility of en face OCT for the detection of clinically unsuspected retinal neovascularization in patients with diabetic retinopathy," Ophthalmology Retina 7, 683-691 (2023).
- 33. T. Hwang, A.-L. Wu, Y. Guo, et al., "Wide-field OCTA Quantified Peripheral Nonperfusion Areas Predict the Risk of Subclinical Neovascularization," Research Square, rs. 3. rs-6182918 (2025).
- 34. T. Hirano, S. Kakihara, Y. Toriyama, et al., "Wide-field en face swept-source optical coherence tomography angiography using extended field imaging in diabetic retinopathy," British Journal of Ophthalmology 102, 1199-1203 (2018).
- 35. E. S. Lu, Y. Cui, R. Le, et al., "Detection of neovascularisation in the vitreoretinal interface slab using widefield swept-source optical coherence tomography angiography in diabetic retinopathy," British Journal of Ophthalmology 106, 534-539 (2022).
- 36. L. Fang, D. Cunefare, C. Wang, et al., "Automatic segmentation of nine retinal layer boundaries in OCT images of non-exudative AMD patients using deep learning and graph search," Biomedical optics express 8, 2732-2744 (2017).
- 37. X.-n. Wang, Z. Guan, B. Qian, et al., "A deep learning system for the detection of optic disc neovascularization in diabetic retinopathy using optical coherence tomography angiography images," The Visual Computer 41, 1293-1302 (2025).